Oxygen Enhanced- and Dynamic Contrast Enhanced- Optoacoustic Tomography provide surrogate biomarkers of tumour vascular function, hypoxia and necrosis.

Authors: M R Tomaszewski[1,2], M Gehrung[1,2,3], J Joseph[1,2], I Quiros-Gonzalez[1,2], J A Disselhorst[3] and S E Bohndiek[1,2] *

Affiliations: [1]Department of Physics and [2]Cancer Research UK Cambridge Institute, University of Cambridge, [3]Werner Siemens Imaging Center, Preclinical Imaging and Radiopharmacy, University of Tuebingen, Germany

Running title: Optoacoustic tomography measures tumour vascular function

Keywords: optoacoustic tomography, tumour microenvironment, perfusion, hypoxia, necrosis

Word Count: 5835 excluding abstract

Figure Count: 7

Corresponding Author (*): *Address*: Department of Physics, Cavendish Laboratory, JJ Thomson Avenue, Cambridge, CB3 0HE, U.K. and Cancer Research UK Cambridge Institute, Li Ka Shing Centre, Robinson Way, Cambridge, CB2 0RE, U.K.. *Phone*: +44 1223 337267; *Fax*: +44 1223 337000; *Email*: seb53@cam.ac.uk.

Abstract:

Measuring the functional status of the tumour vasculature, including blood flow fluctuations and changes in oxygenation is important in cancer staging and therapy monitoring. Current clinically approved imaging modalities suffer long procedure times and limited spatio-temporal resolution. Optoacoustic tomography (OT) is an emerging clinical imaging modality that overcomes these challenges; by acquiring data at multiple wavelengths, OT can interrogate haemoglobin concentration and oxygenation directly, and resolve contributions from injected contrast agents. To establish the potential for OT to be used for rapid, multi-parametric, non-invasive assessment of the tumour vasculature, we tested whether two dynamic OT techniques, oxygen enhanced (OE) and dynamic contrast enhanced (DCE)-OT, could provide surrogate biomarkers of tumour vascular function, hypoxia and necrosis. We found that vascular maturity leads to changes in vascular function that affect tumour perfusion, modulating the DCE-OT signal. Perfusion in turn regulates oxygen availability, driving the OE-OT signal. In particular, we demonstrate for the first time a strong per-tumour and spatial correlation between imaging biomarkers derived from these *in vivo* techniques and tumour hypoxia quantified *ex vivo*. Our findings suggest that OT may in the future offer significant advantage for localised imaging of tumour response to vascular targeted therapies when compared to existing clinical DCE methods.

Introduction: Angiogenesis, the growth of new blood vessels from surrounding host vasculature, can be a rate limiting process in tumour development and progression. The resulting tumour vasculature is often chaotic and tortuous, leading to high intra-tumoural heterogeneity in vascular density and function (1). A high density of tumour vasculature does not necessarily translate into efficient oxygen and nutrient transport (2). Diffusion-limited hypoxia emerges early in tumour development, as rapidly proliferating cancer cells experience a gradient of hypoxia with increasing distance from the nearest perfused blood vessel (3). Perfusion-limited (or 'cycling') hypoxia occurs in cells close to blood vessels that experience rapid spatio-temporal fluctuations in local oxygen delivery due to highly variable blood flow (4). Hypoxia in solid tumours has been associated with both chemo- and radio-resistance (4), as well as poor prognosis (5,6). Furthermore, anti-angiogenic and vascular disrupting therapies are under active clinical development, with highly variable rates of success (7,8). A rapid test to probe the functional status of the tumour vasculature, including blood flow fluctuations and changes in oxygenation, could therefore improve cancer patient management, for example: in distinguishing benign from malignant tumours; in monitoring response to chemo- and radio-therapy; and in aiding development of novel vascular targeted therapies (1).

Non-invasive imaging of tumour vascular function in the clinic usually requires administration of an exogenous untargeted contrast agent followed by longitudinal imaging of wash-in and wash-out kinetics, referred to as Dynamic Contrast Enhanced (DCE) imaging (9). DCE magnetic resonance imaging (MRI) has been broadly applied to interrogate tumour perfusion by tracking the dynamics of an injected Gadolinium-based small molecule contrast agent (10). Unfortunately, an increasing number of reports suggesting long-term toxicity of Gadolinium chelates (11) may limit future use and typical voxel sizes of ~2 x 2 x 4 mm^3 (12) limit interrogation of spatial heterogeneity (5). To avoid the use of contrast agents, label-free MRI techniques that are sensitive to perfusion such as arterial spin labelling (ASL) may be used, however, ASL can suffer from low signal-to-noise ratio, typically requiring voxel sizes of over ~3 x 3 x 4 mm^3 in patients (13). A more established MRI technique is blood oxygen

level dependent (BOLD) MRI, sensitive to deoxyhaemoglobin content, which can reach sub-milimetre in-plane spatial resolution and temporal resolution of < 10 secs clinically (14). The BOLD signal appears to reflect tumour perfusion and hypoxia, based on correlations with immunohistochemistry (15)and can be applied, for example, to indicate prognosis in chemo- and radio- therapy (14,16). Despite this promise, attempts to directly correlate the BOLD and DCE-MRI signals have shown no significant relationship(17) and it has been suggested that some ambiguity remains in the biological interpretation of the BOLD signal (14,18).

Considering other clinical imaging modalities, positron emission tomography (PET) contrast agents are available clinically for visualisation of vascular function (e.g. $H_2^{15}O$) and hypoxia (e.g. ^{18}F-MISO). While these approaches benefit from the exquisite sensitivity of PET, difficulties arise from the fundamental spatial resolution limits(19) and the requirement to administer a radiopharmaceutical, which is a particular challenge for short-half-life agents such as ^{15}O ($t_{1/2}$ ~ 2 min)(20). A more cost-effective option may be possible with diffuse optical spectroscopic imaging, which measures concentrations of oxy- and deoxy-haemoglobin as surrogate markers of hypoxia and is in clinical trials (21), though this all-optical imaging approach suffers from very poor spatial resolution (~1 cm). A cost-effective and high-resolution solution could be available using DCE ultrasound with gas-filled microbubbles as an exogenous contrast agent(22), yet safety concerns related to injection of microbubbles have been raised in patients(23). Thus, there remains a need for cost-effective, non-invasive imaging of tumour vascular function with high spatio-temporal resolution, ideally available without contrast agent administration.

Optoacoustic Tomography (OT) is an emerging imaging modality (24) that is currently in clinical trials (25). OT reveals the distribution of tissue optical absorption in real time (26). Since the optical absorption spectra of oxy- and deoxy-haemoglobin are distinct, acquiring OT data at multiple wavelengths makes it possible to derive imaging biomarkers that relate to total haemoglobin concentration (THb) and oxygenation (SO_2). These imaging biomarkers provide complementary haemodynamic information to those measured clinically with DCE-based

techniques and also the label-free MRI-based techniques introduced above. OT has been shown to monitor the evolution of tumour vasculature during disease development (27,28) and to detect response to vascular targeted therapies (29,30). OT has also been combined with DCE ultrasound (31,32) showing relationships between haemoglobin parameters and perfusion metrics. For these reasons, OT has already been deployed in clinical studies in breast, ovarian and prostate cancers among others, achieving localised imaging at depths of up to 7 cm with spatial resolution of 500 μm or better and wavelength tuning rates of up to 100 Hz (25). Importantly, numerous clinical trials are underway world-wide, which are beginning to show great promise for the technology (despite the aforementioned depth limitations) for detecting tumour vascularisation and differentiating benign and malignant lesions, particularly in the breast (33–35).

In addition to the 'static' measurements of haemoglobin concentration and oxygenation available with existing OT, new techniques have recently emerged that directly report on vascular maturity and function. Inspired by clinically approved Oxygen Enhanced (OE) MRI methods, OE-OT(36) measures the change in haemoglobin oxygenation following a change in respiratory gas from air to 100% oxygen. Contrary to the static measurement of oxygenation, these 'dynamic' OE-OT biomarkers have been shown to correlate with histopathological analysis of tumour vascular function and substantially outperform the static biomarkers in terms of robustness and repeatability(36). DCE-OT is also available, using the clinically approved fluorescent agent Indocyanine Green (ICG) as an untargeted blood pool agent(37). Taking multi-wavelength OT data over time makes it possible to separate ICG signals from oxy- and deoxy-haemoglobin, giving the potential to extract spatially resolved relationships between tumour oxygenation and tumour perfusion in a clinical setting using non-toxic, non-invasive OT imaging.

The purpose of the present study was to evaluate the potential of OT to be used for rapid, multi-parametric, non-invasive assessment of tumour vascular function, hypoxia and necrosis. Here, we perform co-registered OE-OT and DCE-OT in two tumour models, showing

for the first time a quantitative spatial per-pixel correlation between OT metrics derived *in vivo* and the histopathological assessment of vascular maturity and tissue hypoxia *ex vivo*. Furthermore, we resolved the key determinants of OE-OT response in terms of oxygen delivery via the blood supply and oxygen demand in the tissue. Our findings suggest that OE-OT and DCE-OT derived imaging biomarkers can be used as surrogate measures of tumour perfusion and hypoxia. We also note that OE-OT may provide a label-free alternative to DCE approaches for evaluating tumour perfusion that can be readily implemented into the imaging protocol of the emerging clinical optoacoustic technology thanks to its negligible toxicity risk.

Materials and Methods:

Animal Experiments

All animal procedures were conducted in accordance with project (70-8214) and personal licenses (IDCC385D3) issued under the United Kingdom Animals (Scientific Procedures) Act, 1986 and were approved locally under compliance form number CFSB0671. Subcutaneous tumours were established in male BALB/c nude mice (Charles River). $1.5x10^6$ PC3 prostate adenocarcinoma cells suspended in a mixture of 50μL phosphate buffered saline (PBS) and 50μL matrigel (354248, Corning) were inoculated subcutaneously in both lower flanks of n=9 mice (resulting in n=18 tumours). $1x10^6$ K8484 mouse pancreatic adenocarcinoma cells suspended in 100 μL PBS were inoculated subcutaneously in both lower flanks of a further n=4 mice (resulting in n=7 tumours). The K8484 cells[38] were derived from a pancreatic adenocarcinoma of a transgenic mouse model[39,40] and were kindly donated by Prof. Duncan Jodrell's lab at the CRUK Cambridge Institute, providing validation of the findings in a model of distinct morphology to the prostate tumours. Authentication of PC3 cells using Genemapper ID v3.2.1 (Genetica) by STR Genotyping (1/2015) showed 94% match. No authentication was performed in K8484 cells. Both cell types were mycoplasma tested by RNA-capture ELISA prior to use (PC3, 13/03/2017); K8484, 05/09/2017). Cells were used at 4 passages from thawing from frozen stocks. Tumour growth was monitored by callipers and imaging was performed when tumours reached ~8mm in any linear dimension.

To investigate the effect of vascular disruption on the optoacoustic measurements and evaluate its relationship with vascular maturity, $1.5x10^6$ PC3 prostate adenocarcinoma cells were inoculated as described above in a further n=8 mice (resulting in n=16 tumours). In 4 animals both tumours could not be visualised in a single imaging slice, resulting in 4 tumours being excluded, leaving n=12 tumours for analysis. Combretastatin 4A Phosphate (CA4P, C7744, Sigma-Aldrich), a potent Vascular Disrupting Agent with well-established efficacy in preclinical models was used (30,41,42) . When tumours reached ~8mm linear dimension, mice were randomly allocated into two groups: treated (CA4P, 8 mL/kg of 12.5mg/mL solution

dosed intraperitoneally to achieve a dose of 100mg/kg, n=7 tumours, 4 mice), and vehicle (PBS 8ml/kg intraperitoneally, n=5 tumours, 4 mice).

Optoacoustic Tomography (OT)

A commercial multispectral optoacoustic tomography (MSOT) system (inVision 256-TF, iThera Medical GmbH) was used for this study[43]. Briefly, a tunable optical parametric oscillator pumped by an Nd:YAG laser provides excitation pulses with a duration of 9ns for wavelengths ranging from 660nm to 1300nm at a repetition rate of 10Hz, wavelength tuning speed of 10ms and a peak pulse energy of 90mJ at 720nm. Ten arms of a fibre bundle provide uniform illumination of a ring-shaped light strip of approximately 8mm width. For ultrasound detection, 256 toroidally focused ultrasound transducers with a centre frequency of 5MHz (60% bandwidth), organized in a concave array of 270 degree angular coverage and a radius of curvature of 4cm, are used.

Mice were prepared for OT according to our standard operating procedure[44]. Briefly, mice were anaesthetised using <3% isoflurane, placed on a heat pad, and a catheter (home-made with 30G needle) was placed in the tail vein and fixed in place using tissue glue (TS1050071F, TissueSeal). The mouse was subsequently moved into a custom animal holder (iThera Medical) wrapped in a thin polyethylene membrane, with ultrasound gel (Aquasonic Clear, Parker Labs) used to couple the skin to the membrane. The holder was placed within the imaging chamber of the MSOT system filled with degassed heavy water (617385, Sigma-Aldrich) maintained at 36°C, with the end of the catheter line available outside of the imaging chamber for contrast agent injection. Heavy water was used due to other studies performed in parallel on the MSOT system and is not essential to the study described here since the optical absorption of water and heavy water is similar in the spectral range interrogated.

Mice were allowed to stabilise their physiology for 15 minutes within the system prior to initialisation of the scan and their respiratory rate was then maintained in the range 70-80bpm with ~1.8% isoflurane concentration for the entire scan. The respiration rate was

monitored by observing the breathing motion of the animal using a video feed from an optical camera positioned within the imaging chamber and counting the breaths over a minute using a stopwatch. We first performed Oxygen Enhanced Optoacoustic Tomography (OE-OT) (36), in which the breathing gas was switched manually from medical air (21% oxygen) to pure oxygen (100% oxygen) using separate flow meters (according to the schedule in Supplementary Figure S1). A single slice was chosen for imaging showing the largest cross-sectional area of the tumours on both flanks where possible. Images were acquired in the single slice using 10 wavelengths (700, 730, 750, 760, 770, 800, 820, 840, 850, 880 nm) and an average of 6 pulses per wavelength; an entire single slice multi-wavelength data acquisition was 5.5s in duration. In the CA4P and vehicle treated mice, where imaging was performed twice, the imaging slice in the second session was chosen to be as close as possible to the first one by visual alignment to the reconstructed images of the first scan.

Following OE-OT, the breathing gas was switched back to medical air and after 10 minutes allowed for equilibration, the Dynamic Contrast Enhanced (DCE) OT was initiated in the same imaging slice. Images were acquired using 5 wavelengths (700, 730, 760, 800, 850 nm) and an average of 10 pulses. After 1 minute of continuous imaging to establish the baseline signal, a bolus of Indocyanine Green (ICG, 40nmol/20g mouse in PBS)(45) was injected intravenously through the catheter, followed by a pulse of PBS to flush the line. OT was continued for a further 15 minutes to sample the enhancement curve.

All mice underwent the full OT procedure at least once. Mice receiving CA4P or vehicle were imaged at 48h before treatment to ensure clearing of the injected contrast agent and then again at 4h after treatment.

Histopathologic Tumour Staining

Following the last OT procedure, mice were immediately sacrificed by cervical dislocation while still under anaesthesia. The tumours were then excised, taking care for the orientation to be preserved, and cut in half along the imaging plane. The top and left hand side of the

tumours were marked with green and red tissue marking dyes (RCD-0727-3, RCD-0727-5, Cell Path) to later indicate the orientation of histopathologic sections relative to the *in vivo* imaging procedure. One half was then fixed in neutral buffered 10% formalin for 24h prior to paraffin embedding. Fixed blocks were sectioned at 3µm thickness at 4 separate levels within the tumour spaced by 500µm apart. Haematoxylin and eosin (H&E) staining and immunohistochemistry were performed. Adjacent sections from each of the 4 levels were stained with: CD31 (anti-mouse, BD Biosciences, 553370) to indicate vessel density; alpha smooth muscle actin (ASMA) (anti-mouse, Abcam, ab5694) to indicate smooth muscle coverage; and CAIX (anti-human, BioScience Slovakia, AB1001) to indicate hypoxic regions. We also performed pimonidazole staining for hypoxia in a representative tumour to qualitatively assess the reliability of CAIX staining for hypoxia visualisation in the PC3 model. 60mg/kg pimonidazole hydrochloride (Hypoxyprobe) in PBS was injected intraperitoneally 60 minutes before sacrifice. IHC staining (Mab-1 antibody, 4.3.11.3, Hypoxyprobe) was performed on the sections. Spatial co-localisation between CAIX and pimonidazole staining was observed (Supplementary Figure S2). All immunostainings were performed with DAB as substrate. All sections were digitized at 20x with an Ariol System (Aperio Technologies Ltd).

Optoacoustic Tomography Image Analysis

All OT analysis was performed in MATLAB 2017b (Mathworks) using custom software. OT images were reconstructed using an acoustic backprojection algorithm (iThera Medical) with an electrical impulse response correction, to account for the frequency dependent sensitivity profile of the transducers[46], and a speed-of-sound adjustment, to focus the images. Images were reconstructed with a pixel size of 75µm x 75µm, which is approximately equal to half of the in-plane resolution of the InVision 256-TF, to facilitate region drawing. It should be noted that the out-of-plane resolution of this system is approximately 0.9mm [47]. Regions of Interest (ROIs) were drawn manually around the tumour area (excluding the skin) and a healthy, well vascularised tissue region around the spine, in the 800nm (isosbestic)

image taken from the first frame of the OE-OT scan. The reconstructed images were downsampled to 200µm x 200µm pixel size for further analysis, to improve response classification, as described below.

For OE-OT analysis, a pseudoinverse matrix inversion (pinv function in MATLAB 2017b) was used for spectral unmixing of the relative weights of oxy- [HbO_2] and deoxy-haemoglobin [Hb] independently in each pixel. Since OT is not able to accurately measure the absolute SO_2 without the precise knowledge of optical energy distribution, we denote the approximate oxygenation metric derived in this study as the apparent SO_2^{MSOT} rather than absolute SO_2. SO_2^{MSOT} was computed as the ratio of HbO_2 to total haemoglobin THb=[HbO_2+Hb]. Average SO_2^{MSOT} was calculated in each pixel for air and oxygen breathing periods and denoted SO_2^{MSOT} (Air) and SO_2^{MSOT} (O_2) respectively. The amplitude of response to the oxygen gas $\Delta SO_2^{MSOT} = SO_2^{MSOT}$ (O_2) - SO_2^{MSOT} (Air) was calculated for each pixel (illustrated in Figure 1A). The variability of the signal was also assessed by calculating the standard deviation SD_{OE} of the SO_2^{MSOT} values between the individual scans acquired during air breathing. Each pixel was classified as responding to the oxygen challenge if ΔSO_2^{MSOT} exceeded 2 x SD_{OE} (see Supplementary Figure S3). A small fraction of pixels showed artefactual negative Hb or HbO_2 levels due to low signal and were classified as non-responding. The OE Responding Fraction (OE RF) was subsequently calculated for each tumour and scan as the ratio of the number of tumour pixels classified as responding to the total number of pixels in the tumour ROI.

DCE-OT analysis was performed similarly. The same ROIs as for the corresponding OE-OT scans were used, since the imaging was performed in the same slice and the movement of the anaesthetised animal between the scans was negligible. After down-sampling the reconstructed image, linear spectral unmixing as above was performed for HbO_2, Hb and ICG. The amplitude of ICG enhancement, ΔICG, was quantified as the difference between the average baseline ICG signal and the maximum signal recorded in the first 3

minutes after injection (illustrated Figure 1A) to capture the perfusion rather than accumulation effect of the dye. Variability of the ICG signal was also measured as the standard deviation of the individual images acquired before contrast agent injection (SD_{DCE}). Each pixel was then classified as enhancing when ΔICG exceeded 2 x SD_{DCE} (see Supplementary Figure S3) with artefactual, negative pixels classified as non-enhancing. DCE Responding Fraction (DCE RF) was computed accordingly for each tumour.

Correlations between OE and DCE signals were calculated for each tumour on a per-pixel basis. The results presented are from all mice (n=12+18 tumours). The small fraction of pixels showing artefactual SO_2^{MSOT} or ICG signal values were excluded from the correlation analysis. Spearman rank correlation coefficient was calculated (MATLAB) and quoted, due to the apparent non-linear monotonic relationship between the metrics.

Histopathologic Image Analysis and Data Co-registration

For each tumour, 4 sections were analysed (see 'Histopathologic Tumour Staining'). Necrosis was identified from H&E sections using a Convolution Neural Network (CNN) approach. The schematic of the CNN layer architecture is presented in Supplementary Figure S4. The viable and necrotic patches of H&E sections for training the model were identified manually. A threshold of 0.5 was applied to the necrosis score maps to discriminate the necrotic from viable regions as the probabilistic output had a range from 0 to 1, meaning that values below or above 0.5 have a higher likelihood of being viable or necrotic tissue respectively. The necrotic fraction was quantified as the ratio of the total necrotic area to total tumour area across a whole section. Model performance was assessed by qualitative comparison to H&E sections, an example of which is demonstrated in Supplementary Figure S5, and quantitative comparison to results of manual segmentation, performed in Imagescope (Aperio Technologies Ltd). A strong, significant correlation was observed between the model and manual quantification (r=0.75, p<0.0001, see Supplementary Figure S6).

Haemorrhagic areas were identified in H&E sections based on their colour. Quantification of haemorrhagic fraction was performed automatically using Halo (Indica Labs) image analysis software. Analysis of CD31 and ASMA coverage was also performed using Halo software, quantifying the CD31 positive area (to measure the amount of vasculature), as well as the CD31 positive areas that were also positive for ASMA in adjacent sections to identify mature vasculature with smooth muscle coverage(2). The fraction of area positive for both CD31 and ASMA to the CD31 positive area was quoted as a metric. CAIX analysis was performed using custom code written in MATLAB. The areas of CAIX positive staining were identified based on colour deconvolution(48) of the antibody, cell nuclei and background. The correct colours for the 3 classes were computed by manually outlining example areas in two sections. CD31/ASMA analysis was performed in the CA4P/vehicle treated cohort (n=12), to increase the vascular maturity range probed. The CAIX and necrosis analysis was performed in the other cohort only (n=18), as the different experimental protocol (2 imaging sessions for CA4P cohort, 1 for untreated cohort) made the histology datasets not eligible to be combined.

To evaluate the relationship between OT metrics of vascular function and histopathologic assessment of tissue hypoxia, point set registration was performed with points determined by the applied tissue marking dyes(49).

The ΔSO_2^{MSOT} and ΔICG OT images were then compared spatially to CAIX sections. Kernel density estimation, assuming a bimodal intensity distribution with low and high values, was applied on pooled CAIX stain intensity values across all tumours to obtain a discriminative threshold for binarisation of stain intensity in individual sections. The binarised CAIX and necrosis maps were overlaid, and the necrotic areas were excluded from the analysis. Mean ΔSO_2^{MSOT} and ΔICG values in CAIX positive and negative viable regions were then calculated. The differences between the ΔSO_2^{MSOT} and ΔICG values in the CAIX positive and negative regions were then extracted for each tumour, with a value significantly different from 0 taken as a measure of differential response. This informed on spatial co-localisation and co-occurrence of high/low ΔSO_2^{MSOT} with negative/positive CAIX regions. It should be noted that

this approach to image co-registration is subject to human error in tissue handling and sectioning, which leads to a high rate of exclusion for the analysis. Out of the 18 tumours analysed in the cohort, 8 had to be excluded due to failure of the registration, arising from distorted or torn tissue sections, resulting in misplaced tissue marking dyes, which in turn obstructed accurate registration of the image pairs.

Statistical Analysis

All errors are quoted as the standard error on the mean unless otherwise stated. All statistical analyses were performed in OriginPro 9 (OriginLab). Paired two-tailed t-test compared different metrics in each tumour and changes in parameters due to CA4P treatment; unpaired two-tailed t-test assuming equal variances compared between cohorts. One-tailed t-test was used to assess whether the differences in OT parameters between low and high CAIX staining regions are significantly above 0 for the co-registered histopathology and OT image analysis. Only the last scan immediately before sacrifice was used for correlations with histology, and Pearson rank test was performed to assess the significance. $p < 0.05$ was considered statistically significant.

Results:

Oxygen Enhanced (OE) and Dynamic Contrast Enhanced (DCE) OT responses are strongly correlated.

Using our intrinsically co-registered OE-OT and DCE-OT data, we first sought to examine the spatial correlations between the tumour OE and DCE responses. The amplitudes of these responses, ΔSO_2^{MSOT} (Figure 1A, C) and ΔICG (Figure 1B, D) respectively, were compared on a per-pixel basis. Highly significant correlations (p value $<10^{-6}$ in all cases) were observed between these two metrics (Figure 1E). The correlation deviates from linearity for the extreme values, suggesting Spearman rank correlation coefficient as a more informative estimate of the relationship (Figure 1E). While very strong correlations between OE and DCE response were observed in both tumour cohorts (Spearman r=0.64±0.02, n=30 PC3 tumours; Spearman r=0.65±0.07, n=7 K8484 tumours), no correlation was observed to the static metrics of SO_2^{MSOT}(Air) or SO_2^{MSOT}(O_2) measured at baseline, indicating that these metrics are not sensitive to tumour perfusion (Spearman r=-0.16±0.05 and r=-0.11±0.05 for SO_2^{MSOT} (Air) and SO_2^{MSOT} (O_2) respectively for PC3, n=30 PC3 tumours, r=-0.04±0.09 and r=0.25±0.09 respectively for K8484). The correlations for all tumours analysed are summarised in Figure 1F.

ICG retaining pixels in DCE-OT show weak or no OE-OT response.

Examining the DCE-OT data in greater depth, it was clear that two classes of pixels showing distinct ICG kinetics were present. The first such group, referred to as 'clearing' consistently showed an obvious enhancement peak followed by exponential clearance of the contrast down to a plateau (Figure 2A and 2B, blue). The second such group, referred to as 'retaining' showed an enhancement after injection, but displayed no clearance; the level of signal either remained high and stable over the duration of the experiment, or even increased gradually (Figure 2A and 2B, red). As might be expected based on established differences in vascular maturity(36), clearing regions tended to be more prevalent in the rim than the core of

the tumour, with the fraction of the rim occupied by clearing pixels being significantly higher than the corresponding fraction of the core (0.51±0.04 vs. 0.39±0.05, p=0.002, n=30 PC3 tumours. 0.44±0.13 vs. 0.16±0.06, p=0.01, n=7 K8484 tumours).

Interestingly, the OE-OT responses of these two distinct classes of DCE response also showed significant differences (Figure 2C). Retaining regions demonstrate weaker OE response (Figure 2D) and have a significantly lower OE Responding Fraction than Clearing regions (0.55±0.05 vs. 0.25±0.02, $p<10^{-5}$, n=30 PC3 tumours). The retaining regions also show a weaker correlation between the ΔSO_2^{MSOT} and ΔICG (Figure 2E) than the clearing regions (0.57±0.03 vs. 0.44±0.04, p=0.007).

Tumour DCE-OT signal is driven predominantly by vascular maturity while OE-OT is also strongly related to hypoxia and necrosis.

The relationships observed between OE-OT and DCE-OT suggested that similar vascular characteristics may underpin their responses. We next broadly explored the correlations between the *in vivo* OT responses and the *ex vivo* histopathological analysis relating to vascular maturity (ASMA coverage of CD31 positive blood vessels), hypoxia (CAIX positivity) and tumour viability (necrosis assessed with H&E) on a per-tumour basis in PC3 tumours, where our study was sufficiently well powered to identify significant correlations.

Vascular maturity (Figure 3A) showed a significant positive correlation with both OE Responding Fraction (OE RF, r=0.58, p=0.048, n=12 PC3 tumours) and DCE Responding Fraction (DCE RF, r=0.78, p=0.002, n=12 PC3 tumours) (Figure 3B, C). As could be expected given the direct influence of vascular maturity on vessel function and subsequently on perfusion, a higher and more significant correlation was observed for DCE RF than for OE RF.

A significant negative correlation was found between hypoxia (based on CAIX positive area fraction) and OE RF (Figure 4A, Supplementary Figure S7; r=-0.68, p=0.002, n=18 PC3 tumours). The negative correlation between hypoxia and DCE RF was weaker (Figure 4A, Supplementary Figure S7; r=-0.49, p=0.04, n=18 tumours). A negative correlation was also

observed between OE RF and the tumour necrotic fraction (Figure 4B, Supplementary Figure S8; r=-0.56, p=0.016, n=18 tumours), however, no significant relationship was seen for DCE RF (Figure 4B, Supplementary Figure S8; r=-0.42, p=0.08, n=18 tumours).

Given the strong relationship between hypoxia and OE-OT response, we investigated further by examining the spatial co-localisation of high ΔSO_2^{MSOT} and low CAIX signals. Taking each CAIX stained section (Figure 5A) and H&E stained section (Figure 5B), we performed an image co-registration and down-sampled the spatial resolution of the CAIX image (binarised into high and low staining regions) to match that of the *in vivo* OT image (Figure 5C). The resulting co-registered CAIX data was then compared to ΔICG (Figure 5D) and ΔSO_2^{MSOT} (Figure 5E) on a per-pixel basis. Where successful co-registration was possible (n=10 PC3 tumours, see Methods), the analysis revealed that areas of low CAIX staining (considered to reflect low tissue hypoxia) were associated with a notably higher mean ΔSO_2^{MSOT} level than the areas of high CAIX staining (Figure 5E). The difference between average ΔSO_2^{MSOT} taken in low CAIX compared to that in high CAIX regions was significantly higher than 0 when compared across all tumours (difference=0.014±0.005 vs. 0, p=0.007, n=10 PC3 tumours). The average ΔICG was also significantly higher in normoxic than in hypoxic tumour regions in line with the per-tumour findings (difference=0.42±0.17 vs. 0, p=0.018, n=10 PC3 tumours).

OE-OT and DCE-OT are highly sensitive to treatment with a vascular disrupting agent

Having established relationships between OE-OT and DCE-OT imaging biomarkers with vascular function, hypoxia, and necrosis, we then sought to evaluate their utility in detecting response to a vascular disrupting agent. Imaging studies were performed both before and 4h after administration of the vascular disrupting agent Combretastatin A4 Phosphate. The 4h time point was chosen so as to observe the induced vascular disruption prior to the development of substantial tumour necrosis (30).

The dramatic effect of the treatment on tumour vasculature was confirmed histologically (Supplementary Figure S9). As desired, this was not followed by induction of significant necrosis in the treated tumours (necrotic fraction=0.28±0.09, n=6 vs. 0.18±0.06, n=5 treated vs. vehicle, p=0.38). The induced vascular disruption was qualitatively observed in maps of ΔSO_2^{MSOT} and ΔICG (Supplementary Figure S10A) as well as in the quantification of the kinetic responses in both cases (Supplementary Figure S10B,C). As expected, treated tumours were dominated by ICG retaining areas (as defined in Fig. 2). Clear changes in the spatial distribution of responding pixels could be observed in both OE-OT and DCE-OT images in drug treated tumours (Figure 6A), but not in the vehicle treated ones (Supplementary Figure S11). These changes were reflected in the responding fractions in vehicle and CA4P treated tumours (Figure 6B). OE RF showed a significant decrease between 48h before and 4h after treatment (0.47±0.05 vs. 0.16±0.03, p=0.0005, n=7 PC3 tumours). No significant change was seen in vehicle treated control animals (0.38±0.06 vs. 0.30±0.05, p=0.44, n=5 PC3 tumours). Similarly, DCE RF showed a significant decrease (0.63±0.05 vs. 0.32±0.02, p=0.0001, n=7 PC3 tumours), while control did not (0.74±0.06 vs. 0.68±0.05, p=0.34, n=5 PC3 tumours).

Discussion:

The balance of oxygen supply and demand in solid tumours can be a key determinant of prognosis and response to therapy. The aim of this work was to evaluate the potential of imaging biomarkers accessible using OT to be used in rapid, multi-parametric and non-invasive assessment of tumour vascular function and monitoring response to therapy.

We first examined the relationship between the two OT imaging biomarkers under study: ΔSO_2^{MSOT}, accessible without the introduction of a contrast agent using OE-OT; and ΔICG, requiring administration of the clinically approved and non-toxic contrast agent indocyanine green and imaged through a DCE-OT technique. These dynamic biomarkers were strongly spatially correlated in both tumour models examined, suggesting that perfusion is a strong determinant of response in both techniques. The kinetics of the DCE-OT response also showed strong differences between 'clearing' and 'retaining' regions, the latter of which have been previously described as associated with the enhanced permeability and retention effect in areas of immature and leaky vasculature(50,51). These regions also showed distinct OE-OT responses, with greater ΔSO_2^{MSOT} seen in clearing regions.

We then established how these OT imaging biomarkers were connected with *ex vivo* measurements of vascular function, as well as tumour hypoxia and necrosis; these relationships are summarised in Figure 7. Vascular maturity leads to changes in vascular function that affect tumour perfusion, modulating the DCE-OT signal. Perfusion in turn regulates oxygen availability, driving the OE-OT signal. Insufficient oxygen supply leads to tissue hypoxia and eventually necrosis (4) (Figure 7, bottom row). These relationships, and hence our understanding of the OE and DCE-OT signals, were directly confirmed by the correlations observed between our *in vivo* OT and *ex vivo* histopathological measurements (Figure 7, middle row). The strength of the correlation reflected how closely the individual measurement is linked with the underlying physiological process (Figure 7, top row), overall revealing a complex, yet consistent network of relationships in the tumour vascular microenvironment. These findings indicate that the response for DCE-OT is driven most strongly by perfusion and vascular function, which would be expected

given that ICG shows strong serum binding *in vivo*. The response for OE-OT appears to also be governed strongly by perfusion and vascular function but is further modulated by the tumour oxygen demand. The strong and significant relationships observed between the OE responding fraction and hypoxia area on a per-tumour basis were also confirmed on a spatial per-pixel basis.

Treatment with a potent vascular disrupting agent, Combretastatin A4 Phosphate, was used to induce vascular shutdown, causing a dramatic perfusion drop, resulting in a significant decrease in DCE RF, as expected. Interestingly, the OE RF showed equally high sensitivity to the vascular shutdown, indicating that it could be used as an alternative to the contrast agent-based DCE methods for detecting response to vascular targeted therapies. Both of our surrogate biomarkers were able to sensitively detect response to the vascular targeted therapy.

In line with our previous findings(36), static OT biomarkers such as $SO_2^{MSOT}(O_2)$ and $SO_2^{MSOT}(Air)$ showed little relationship to perfusion or hypoxia. Similar relationships were examined previously comparing tumour oxygenation assessed using static OT with DCE ultrasound(31,32) or pimonidazole staining(52). While some spatial relationships were noted, particularly in relation to the necrotic tumour core, these studies were limited respectively by a lack of histological validation, poor sensitivity of the optoacoustic imaging approach applied and small numbers of biological replicates.

There remain some limitations to the presented work that must be addressed in future studies. From a biological perspective, vascularisation of subcutaneous models differs from that of orthotopic xenografts and spontaneous tumours(53) and may not be entirely representative of the vascular function found clinically in solid tumours. These findings should therefore be validated in orthotopic and transgenic tumour models prior to application of dynamic OT metrics in studies of cancer biology or in the clinic. In our subcutaneous PC3 model, good co-localisation was observed between CAIX and pimonidazole staining, which we took as an indication that CAIX staining indeed reflected hypoxia in this model. While CAIX staining is well-documented to be regulated by the activation of Hypoxia Inducible Factor (HIF-1)(54) and has been widely used for *ex vivo* hypoxia identification, non-specific effects can be

observed in some models, therefore if our findings are to be further validated in other tumour models, it would be prudent to use multiple methods to assess hypoxia *ex vivo*.

Some further limitations exist in the efficient clinical translation of OT and associated imaging biomarkers. Penetration depths of up to 3-7cm (25) have been reported in patients, enabling access to superficial cancer sites, such as those in the breast or head and neck. With the ongoing development of endoscopic probes, imaging organs such as the prostate (55) is also expected to be possible, yet access to some deep seated organs will remain limited even with these technological advances. The localised nature of OT means that it would be most appropriately placed in the patient management pathway after diagnosis or identification of a suspicious lesion using another imaging technique. Light attenuation at depth in tissue poses an additional challenge for signal quantification. Methods available to perform light fluence correction of OT data have received only limited validation *in vivo* (47). Future work is required to directly relate OT data to absorbed optical energy density and enable absolute quantification if desired. However, qualitative features derived from clinical optoacoustic images have also shown significant prognostic value (56).

In summary, we have shown that non-invasive and non-toxic OE-OT and DCE-OT techniques can be used to interrogate tumour vascular function, hypoxia and necrosis. The comprehensive histopathological validation of the OT imaging biomarkers presented here indicates that despite the aforementioned technical challenges that face the technology, OT is capable of providing a unique and rapid insight into the tumour vascular microenvironment. While DCE-OT requires administration of a contrast agent, OE-OT provides a completely non-invasive, label-free measurement; our findings indicate that the oxygen challenge approach could be used as a safe alternative for exogenous contrast injection as it has been used clinically with no associated risk(57). OT is already being tested, with promising results in numerous clinical trials in cancer patients(33–35), despite some technical limitations of the technology. In the future, the low cost, portability and simplicity of OT may offer significant

advantage for localised imaging of tumour response to vascular targeted therapies when compared to existing clinical DCE methods, particularly in the neo-adjuvant setting.

Acknowledgments

References

1. Gillies RJ, Schornack PA, Secomb TW, Raghunand N. Causes and Effects of Heterogeneous Perfusion in Tumors. Neoplasia. 1999;1:197–207.

2. Eberhard A, Kahlert S, Goede V, Hemmerlein B, Plate KH, Augustin HG. Heterogeneity of angiogenesis and blood vessel maturation in human tumors: implications for antiangiogenic tumor therapies. Cancer Res. 2000;60:1388–93.

3. Nagy JA, Chang S-H, Dvorak AM, Dvorak HF. Why are tumour blood vessels abnormal and why is it important to know? Br J Cancer. 2009;100:865–9.

4. Michiels C, Tellier C, Feron O. Cycling hypoxia: A key feature of the tumor microenvironment. Biochim Biophys Acta - Rev Cancer. 2016;1866:76–86.

5. O'Connor JPB, Rose CJ, Waterton JC, Carano RAD, Parker GJM, Jackson A. Imaging Intratumor Heterogeneity: Role in Therapy Response, Resistance, and Clinical Outcome. Clin Cancer Res. 2015;21:249–57.

6. Lundgren K, Holm C, Landberg G. Hypoxia and breast cancer: prognostic and therapeutic implications. Cell Mol Life Sci. 2007;64:3233–47.

7. Gacche RN, Meshram RJ. Angiogenic factors as potential drug target: Efficacy and limitations of anti-angiogenic therapy. Biochim Biophys Acta - Rev Cancer. 2014;1846:161–79.

8. Thorpe PE. Vascular targeting agents as cancer therapeutics. Clin Cancer Res. 2004;10:415–27.

9. O'Connor JPB, Tofts PS, Miles KA, Parkes LM, Thompson G, Jackson A. Dynamic contrast-enhanced imaging techniques: CT and MRI. Br J Radiol. 2011;84 Spec No:S112-20.

10. Paldino MJ, Barboriak DP, Folkman J, Knopp MV, Giesel FL, Marcos H, et al.

Fundamentals of Quantitative Dynamic Contrast-Enhanced MR Imaging. Magn Reson Imaging Clin N Am. 2009;17:277–89.

11. Gulani V, Calamante F, Shellock FG, Kanal E, Reeder SB, International Society for Magnetic Resonance in Medicine. Gadolinium deposition in the brain: summary of evidence and recommendations. Lancet Neurol. 2017;16:564–70.

12. Little RA, Barjat H, Hare JI, Jenner M, Watson Y, Cheung S, et al. Evaluation of dynamic contrast-enhanced MRI biomarkers for stratified cancer medicine: How do permeability and perfusion vary between human tumours? Magn Reson Imaging. 2018;46:98–105.

13. Grade M, Hernandez Tamames JA, Pizzini FB, Achten E, Golay X, Smits M. A neuroradiologist's guide to arterial spin labeling MRI in clinical practice. Neuroradiology. 2015;57:1181–202.

14. Jiang L, Weatherall PT, McColl RW, Tripathy D, Mason RP. Blood oxygenation level-dependent (BOLD) contrast magnetic resonance imaging (MRI) for prediction of breast cancer chemotherapy response: A pilot study. J Magn Reson Imaging. 2013;37:1083–92.

15. Hammond EM, Asselin M-C, Forster D, O'Connor JPB, Senra JM, Williams KJ. The Meaning, Measurement and Modification of Hypoxia in the Laboratory and the Clinic. Clin Oncol. 2014;26:277–88.

16. Rodrigues LM, Howe FA, Griffiths JR, Robinson SP. Tumor R2* is a prognostic indicator of acute radiotherapeutic response in rodent tumors. J Magn Reson Imaging. 2004;19:482–8.

17. Jiang L, Zhao D, Constantinescu A, Mason RP. Comparison of BOLD contrast and Gd-DTPA dynamic contrast-enhanced imaging in rat prostate tumor. Magn Reson Med. 2004;51:953–60.

18.   Howe FA, Robinson SP, McIntyre DJ, Stubbs M, Griffiths JR. Issues in flow and oxygenation dependent contrast (FLOOD) imaging of tumours. NMR Biomed. 2001;14:497–506.

19.   Moses WW. Fundamental Limits of Spatial Resolution in PET. Nucl Instrum Methods Phys Res A. 2011;648 Supplement 1:S236–40.

20.   Lopci E, Grassi I, Chiti A, Nanni C, Cicoria G, Toschi L, et al. PET radiopharmaceuticals for imaging of tumor hypoxia: a review of the evidence. Am J Nucl Med Mol Imaging. 2014;4:365–84.

21.   Tromberg BJ, Zhang Z, Leproux A, O'Sullivan TD, Cerussi AE, Carpenter PM, et al. Predicting responses to neoadjuvant chemotherapy in breast cancer: ACRIN 6691 trial of diffuse optical spectroscopic imaging. Cancer Res. 2016;76:5933–44.

22.   Lassau N, Chami L, Benatsou B, Peronneau P, Roche A. Dynamic contrast-enhanced ultrasonography (DCE-US) with quantification of tumor perfusion: a new diagnostic tool to evaluate the early effects of antiangiogenic treatment. Eur Radiol. 2007;17 Suppl 6:F89-98.

23.   ter Haar G. Safety and bio-effects of ultrasound contrast agents. Med Biol Eng Comput. 2009;47:893–900.

24.   Taruttis a., van Dam GM, Ntziachristos V. Mesoscopic and Macroscopic Optoacoustic Imaging of Cancer. Cancer Res. 2015;75:1548–60.

25.   Zackrisson S, van de Ven SMWY, Gambhir SS. Light in and sound out: emerging translational strategies for photoacoustic imaging. Cancer Res. 2014;74:979–1004.

26.   Dima A, Burton NC, Ntziachristos V. Multispectral optoacoustic tomography at 64, 128, and 256 channels. J Biomed Opt. 2014;19:36021.

27.   Wilson KE, Bachawal S V., Tian L, Willmann JK. Multiparametric spectroscopic photoacoustic imaging of breast cancer development in a transgenic mouse model.

Theranostics. 2014;4:1062–71.

28. Quiros-Gonzalez I, Tomaszewski MR, Aitken SJ, Ansel-Bollepalli L, McDuffus L-A, Gill M, et al. Optoacoustics delineates murine breast cancer models displaying angiogenesis and vascular mimicry. Br J Cancer 2018. 2018;1.

29. Rich LJ, Seshadri M. Photoacoustic Imaging of Vascular Hemodynamics: Validation with Blood Oxygenation Level-Dependent MR Imaging. Radiology. 2015;275:110–8.

30. Dey S, Kumari S, Kalainayakan SP, Campbell J, Ghosh P, Zhou H, et al. The vascular disrupting agent combretastatin A-4 phosphate causes prolonged elevation of proteins involved in heme flux and function in resistant tumor cells. Oncotarget. 2018;9:4090–101.

31. Bar-Zion A, Yin M, Adam D, Foster FS. Functional flow patterns and static blood pooling in tumors revealed by combined contrast-enhanced ultrasound and photoacoustic imaging. Cancer Res. 2016;76:4320–31.

32. Shah A, Bush N, Box G, Eccles S, Bamber J. Value of combining dynamic contrast enhanced ultrasound and optoacoustic tomography for hypoxia imaging. Photoacoustics. 2017;8:15–27.

33. Becker A, Masthoff M, Claussen J, Ford SJ, Roll W, Burg M, et al. Multispectral optoacoustic tomography of the human breast: characterisation of healthy tissue and malignant lesions using a hybrid ultrasound-optoacoustic approach. Eur Radiol. 2018;28:602–9.

34. Diot G, Metz S, Noske A, Liapis E, Schroeder B, Ovsepian S V, et al. Multi-Spectral Optoacoustic Tomography (MSOT) of human breast cancer. Clin Cancer Res. 2017;

35. Heijblom M, Piras D, van den Engh FM, van der Schaaf M, Klaase JM, Steenbergen W, et al. The state of the art in breast imaging using the Twente Photoacoustic Mammoscope: results from 31 measurements on malignancies. Eur Radiol.

2016;26:3874–87.

36. Tomaszewski MR, Gonzalez IQ, O'Connor JP, Abeyakoon O, Parker GJ, Williams KJ, et al. Oxygen Enhanced Optoacoustic Tomography (OE-OT) Reveals Vascular Dynamics in Murine Models of Prostate Cancer. Theranostics. 2017;7:2900–13.

37. Weber J, Beard PC, Bohndiek SE. Contrast agents for molecular photoacoustic imaging. Nat Methods. 2016;13:639–50.

38. Courtin A, Richards FM, Bapiro TE, Bramhall JL, Neesse A, Cook N, et al. Anti-Tumour Efficacy of Capecitabine in a Genetically Engineered Mouse Model of Pancreatic Cancer. Algül H, editor. PLoS One. 2013;8:e67330.

39. Olive KP, Jacobetz MA, Davidson CJ, Gopinathan A, McIntyre D, Honess D, et al. Inhibition of Hedgehog signaling enhances delivery of chemotherapy in a mouse model of pancreatic cancer. Science. 2009;324:1457–61.

40. Schreiber FS, Deramaudt TB, Brunner TB, Boretti MI, Gooch KJ, Stoffers DA, et al. Successful growth and characterization of mouse pancreatic ductal cells: functional properties of the Ki-RASG12V oncogene. Gastroenterology. 2004;127:250–60.

41. Liu L, Su X, Mason RP. Dynamic contrast enhanced fluorescent molecular imaging of vascular disruption induced by combretastatin-A4P in tumor xenografts. J Biomed Nanotechnol. 2014;10:1545–51.

42. Salmon BA, Siemann DW. Characterizing the Tumor Response to Treatment With Combretastatin A4 Phosphate. Int J Radiat Oncol Biol Phys. 2007;68:211–7.

43. Morscher S, Driessen WHP, Claussen J, Burton NC. Semi-quantitative multispectral optoacoustic tomography (MSOT) for volumetric PK imaging of gastric emptying. Photoacoustics. 2014;2:103–10.

44. Joseph J, Tomaszewski MR, Quiros-Gonzalez I, Weber J, Brunker J, Bohndiek SE. Evaluation of Precision in Optoacoustic Tomography for Preclinical Imaging in Living

Subjects. J Nucl Med. 2017;58:807–14.

45.   Taruttis A, Morscher S, Burton NC, Razansky D, Ntziachristos V. Fast Multispectral

        Optoacoustic Tomography (MSOT) for Dynamic Imaging of Pharmacokinetics and

        Biodistribution in Multiple Organs. Prow TW, editor. PLoS One. 2012;7:e30491.

46.   Caballero MAA, Rosenthal A, Buehler A, Razansky D, Ntziachristos V. Optoacoustic

        determination of spatio- temporal responses of ultrasound sensors. IEEE Trans

        Ultrason Ferroelectr Freq Control. 2013;60:1234–44.

47.   Brochu FM, Brunker J, Joseph J, Tomaszewski MR, Morscher S, Bohndiek SE.

        Towards Quantitative Evaluation of Tissue Absorption Coefficients Using Light

        Fluence Correction in Optoacoustic Tomography. IEEE Trans Med Imaging.

        2017;36:322–31.

48.   Ruifrok AC, Johnston DA. Quantification of histochemical staining by color

        deconvolution. Anal Quant Cytol Histol. 2001;23:291–9.

49.   Hill DLG, Hawkes DJ, Crossman JE, Gleeson MJ, Cox TCS, Bracey EECML, et al.

        Registration of MR and CT images for skull base surgery using point-like anatomical

        features. Br J Radiol. 1991;64:1030–5.

50.   Onda N, Kimura M, Yoshida T, Shibutani M. Preferential tumor cellular uptake and

        retention of indocyanine green for *in vivo* tumor imaging. Int J Cancer. 2016;139:673–

        82.

51.   Herzog E, Taruttis A, Beziere N, Lutich AA, Razansky D, Ntziachristos V. Optical

        imaging of cancer heterogeneity with multispectral optoacoustic tomography.

        Radiology. 2012;263:461–8.

52.   Gerling M, Zhao Y, Nania S, Norberg KJ, Verbeke CS, Englert B, et al. Real-Time

        Assessment of Tissue Hypoxia *In Vivo* with Combined Photoacoustics and High-

        Frequency Ultrasound. Theranostics. 2014;4:604–13.

53. Eklund L, Bry M, Alitalo K. Mouse models for studying angiogenesis and lymphangiogenesis in cancer. Mol Oncol. 2013;7:259–82.

54. Wykoff CC, Beasley NJ, Watson PH, Turner KJ, Pastorek J, Sibtain A, et al. Hypoxia-inducible expression of tumor-associated carbonic anhydrases. Cancer Res. 2000;60:7075–83.

55. Lediju Bell MA, Guo X, Song DY, Boctor EM. Transurethral light delivery for prostate photoacoustic imaging. J Biomed Opt. 2015;20:036002.

56. Neuschler EI, Butler R, Young CA, Barke LD, Bertrand ML, Böhm-Vélez M, et al. A Pivotal Study of Optoacoustic Imaging to Diagnose Benign and Malignant Breast Masses: A New Evaluation Tool for Radiologists. Radiology. 2018;287:398–412.

57. Moreton FC, Dani KA, Goutcher C, O'Hare K, Muir KW. Respiratory challenge MRI: Practical aspects. NeuroImage Clin. 2016;11:667–77.

Figures with legends:

Figure 1. **Tumour oxygen enhanced optoacoustic tomography (OE-OT) and dynamic contrast enhanced (DCE)-OT responses are strongly correlated.** A strong spatial relationship was observed between the response maps for OE-OT (A) and DCE-OT (B) in both PC3 (top) and K8484 (bottom) tumours. OE and DCE kinetic curves (C,D) were used to quantify metrics as denoted that were then compared in correlation analyses on a per-pixel basis in each tumour. (E) Exemplar per-pixel correlations for each tumour type. (F) When comparing correlations extracted from the entire tumour cohort (each data point represents one tumour), significantly stronger correlations were observed to the dynamic OE-OT metric ΔSO_2^{MSOT} than either static metrics of SO_2^{MSOT} (Air) and $SO_2^{MSOT}(O_2)$. No correlation (correlation coefficient of 0) is indicated with a red dashed horizontal line. Data in (A-E) are exemplars taken from one representative tumour for each type. Data in (F) are taken from the entire tumour cohort (n=30 PC3, n=7 K8484). *** p<0.001 by paired two-tailed t-test. Boxes between 25th and 75th percentile, line at median.
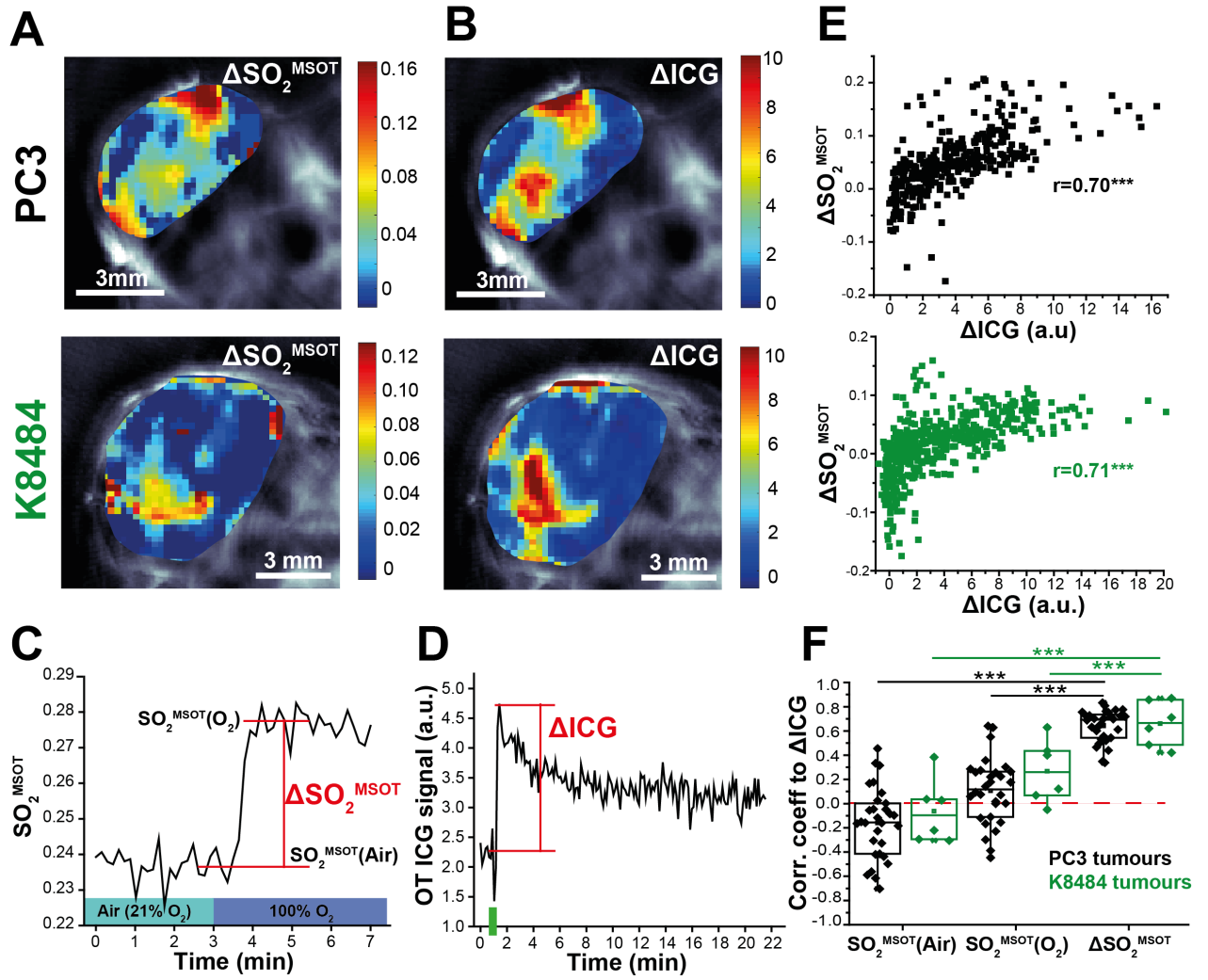
Figure 2. **Two distinct classes of DCE kinetics also possess different OE kinetics.** Spatially distinct regions were segmented showing ICG clearance or retention (A) following injection, according to the DCE-OT response kinetics (B). The retaining regions show little or no OE-OT response (C), reflecting the poorer vascular function in the area. Response maps of OE-OT (D) and DCE-OT (E) are also shown, with the Clearing, Retaining and non-enhancing regions denoted in light blue, red and black regions of interest respectively. These further indicate that the strongest OE response occurs in Clearing regions, as suggested in (C). Data shown are from a representative PC3 tumour.
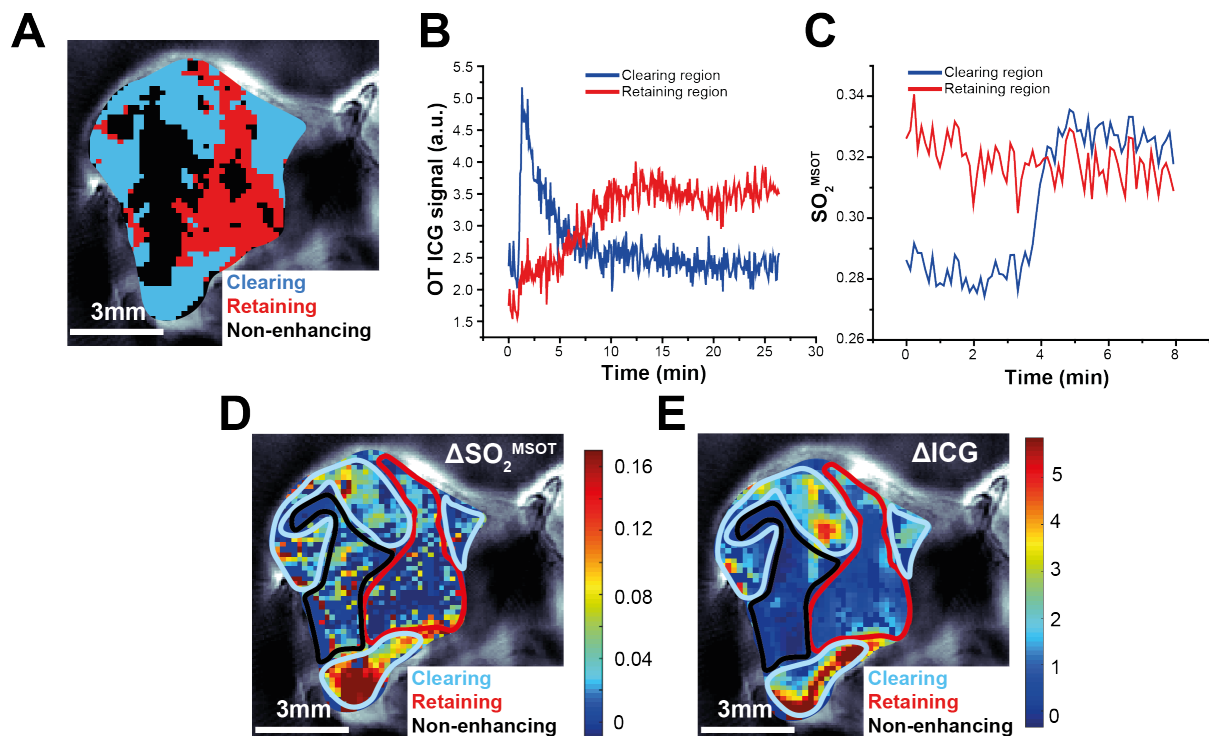
Figure 3. **OE-OT and DCE-OT responses show a significant positive correlation with vascular maturity.** (A) Overlaid CD31 and ASMA stained sections were used to evaluate the fraction of blood vessels positive for ASMA (red on CD31 stained section). The OE Responding Fraction (B) and DCE Responding Fraction (C) both show a significant correlation to tumour vascular maturity (B), with DCE showing a stronger relationship. The analysis includes tumours treated with Combretastatin-A4-Phosphate (red points, n=7 PC3 tumours), which show clearly lower ASMA coverage than vehicle treated tumours (black points, n=5 PC3 tumours). * p<0.05, ** p<0.01 shows the strength of the correlation assessed using a Pearson rank test. Line of best fit with 95% confidence intervals are also shown in the graphs.
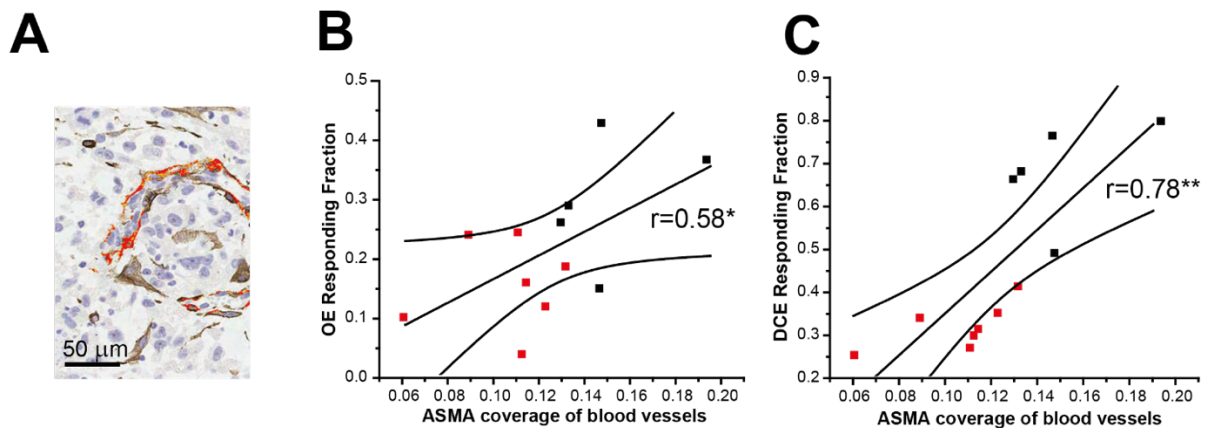
Figure 4. **OE-OT is also strongly related to tumour hypoxia and necrosis.** (A) Representative CAIX stained sections were used to quantify the extent of tumour hypoxia, to which OE-OT response shows a strong inverse correlation, while the DCE-OT response shows a weaker relationship. (B) H&E stained sections were used to quantify the extent of tumour necrosis (green line outlines necrotic area), to which OE-OT again showed a strong inverse correlation, while DCE-OT response was not significant. Analysis shown from n=18 PC3 tumours. n.s. not significant, * p<0.05, ** p<0.01. Line of best fit with 95% confidence intervals are shown in the graphs where significant relationships are identified.
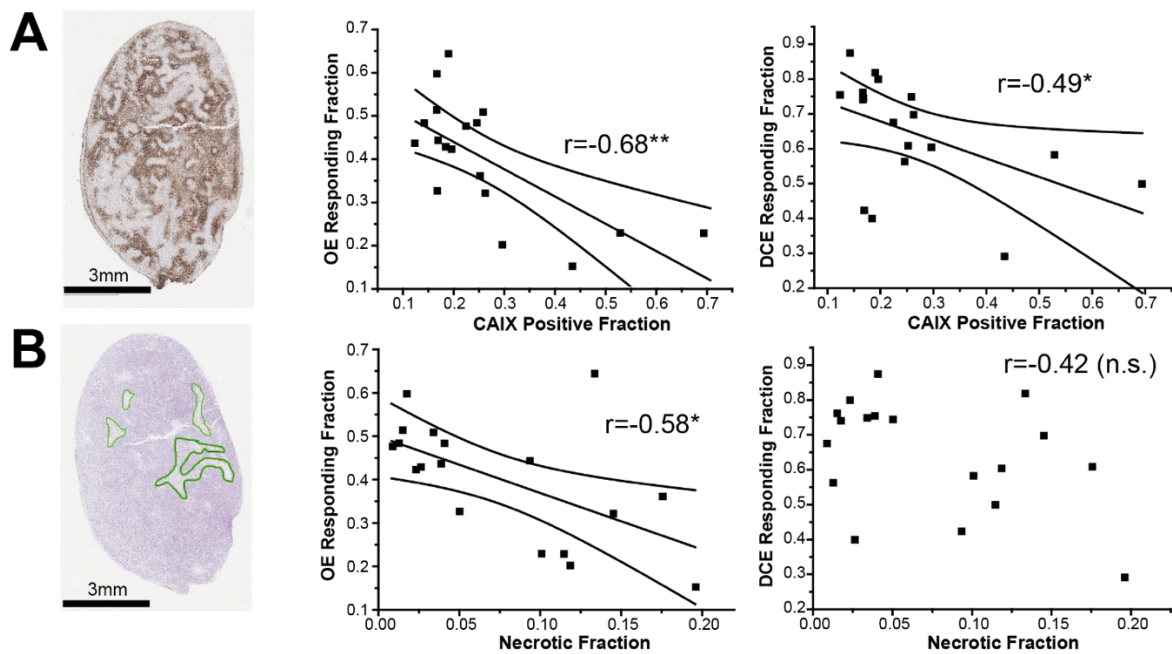
Figure 5. **Spatial co-registration allows comparison of OE-OT and DCE-OT response in hypoxic tumour tissue.** CAIX stained sections (A) were binarised into low and high stain areas. This information was overlaid with necrosis map obtained from H&E sections (B) then co-registered and down-sampled (C) for comparison with the optoacoustic images. DCE-OT ΔICG (D) and OE-OT ΔSO_2^{MSOT} (E) could then be compared to the degree of CAIX staining in viable areas. The box plots show that for the analysed tumours the difference between ΔICG (D) and ΔSO_2^{MSOT} (E) between areas of low and high CAIX hypoxia staining, is significantly higher than 0 (indicated with red dashed line). Images in (A-C) from a representative PC3 tumour. Analysis in (D,E) presented from n=10 PC3 tumours. * p<0.05, ** p<0.01 by one-tailed t-test (deviation from 0). Box between 25th and 75th percentile, line at median.
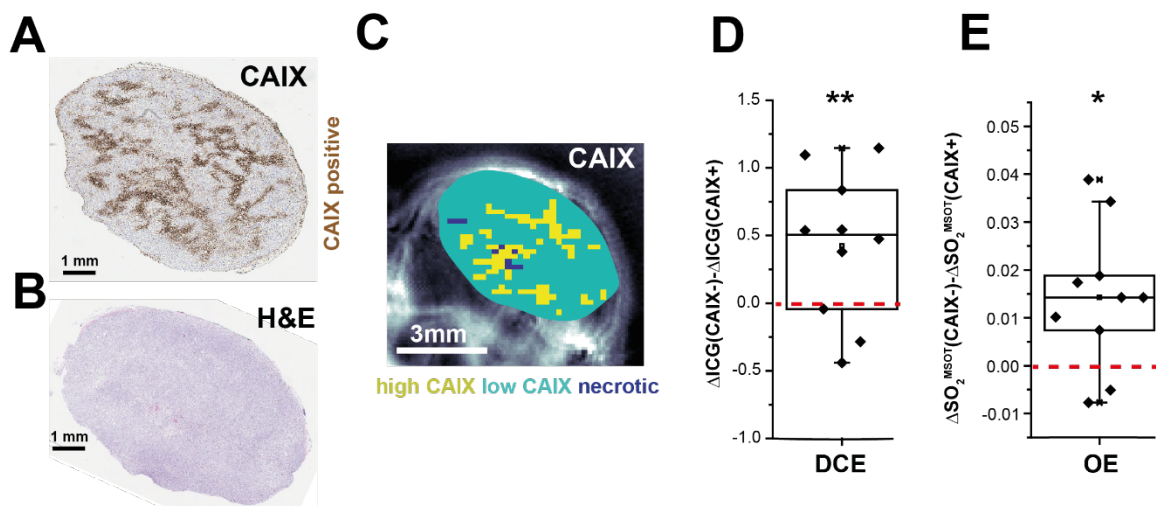
Figure 6. **OE and DCE enhancement show similarly high sensitivity in detecting changes in vascular function.** Both OE Responding Fraction and DCE Responding fraction show a drastic drop due to vascular shutdown caused by the treatment, as seen in representative enhancement maps from a PC3 tumour (A) and in box plot (n=7 treated, n=5 vehicle PC3 tumours). n.s. not significant, *** $p < 0.001$ by paired two-tailed t-test. Box between 25th and 75th percentile, line at median.
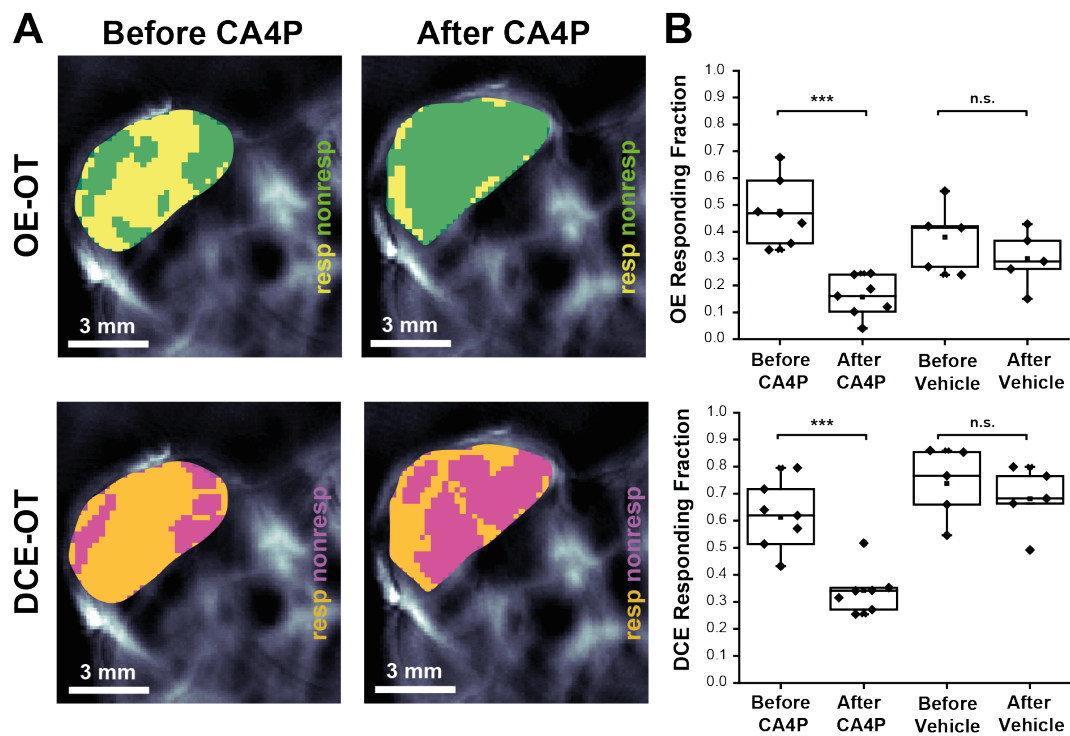
Figure 7. **Summary of the relationships governing tumour physiology that have been established with Optoacoustic Tomography imaging biomarkers.** The physiological relationships underpin the *correlations* that we observed between the *in vivo* and *ex vivo* *measurements* of physiological *processes*. As indicated with the colour bar, the more disconnected the physiological parameters are from each other, the weaker the observed correlations. * $p < 0.05$, ** $p < 0.01$.